Optimized Assembly and Covalent Coupling of Single-Molecule DNA Origami Nanoarrays

Ashwin Gopinath[*,†] and **Paul W. K. Rothemund**[*,†,‡,§]

Departments of [†]Bioengineering, [‡]Computer Science, and [§]Computation & Neural Systems, California Institute of Technology, Pasadena, California 91125, United States

ABSTRACT Artificial DNA nanostructures, such as DNA origami, have great potential as templates for the bottom-up fabrication of both biological and nonbiological nanodevices at a resolution unachievable by conventional top-down approaches. However, because origami are synthesized in solution, origami-templated devices cannot easily be studied or integrated into larger on-chip architectures. Electrostatic self-assembly of origami onto lithographically defined binding sites on Si/SiO$_2$ substrates has been achieved, but conditions for optimal assembly have not been characterized, and the method requires high Mg^{2+} concentrations at which most devices aggregate. We present a quantitative study of parameters affecting origami placement, reproducibly achieving single-origami binding at 94 ± 4% of sites, with 90% of these origami having an orientation within ±10° of their target orientation. Further, we introduce two techniques for converting electrostatic DNA—surface bonds to covalent bonds, allowing origami arrays to be used under a wide variety of Mg^{2+}-free solution conditions.

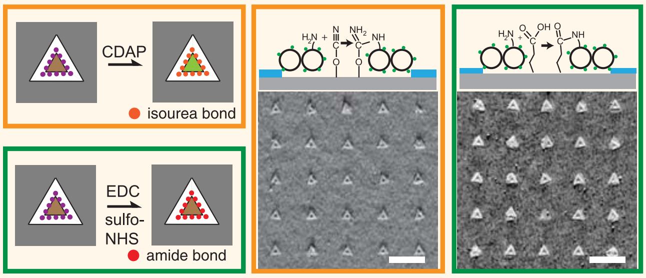

KEYWORDS: DNA nanotechnology · directed self-assembly · single molecule · nanoarray · surface diffusion

Structural DNA nanotechnology[1] allows an experimenter to specify complex nanoscale geometries and to decorate those geometries with arbitrary patterns of functional materials to create devices. In particular, two-dimensional[2] and three-dimensional[3−5] DNA origami provide modular "molecular breadboards" upon which 200 different components can be self-assembled with a resolution of ~6 nm. DNA origami have already been used to assemble prototype electronic[6,7] devices, optical devices,[8−12] biosensing assays,[13−15] and custom single-molecule instruments for answering biological questions.[16−18] Further, origami are being developed as templates[19,20] and as masks[21,22] for new nanolithographies to pattern gold,[7,19] graphene,[22] silicon,[21] and other materials.[20]

Such applications demonstrate the potential of DNA nanostructures for bottom-up fabrication, but characterization and integration of DNA-organized devices have proven difficult, primarily because DNA nanostructures are synthesized in solution. Whether devices are assembled on origami in solution or created after origami deposition, simple surface deposition results in random arrangements of devices with random orientations. Prior to any analysis, device locations must be mapped with an ultramicroscopy such as scanning electron microscopy (SEM) or atomic force microscopy (AFM). For applications which require addressing or integrating devices, such as nanoelectronics,[6] custom patterns of electrodes must be written using e-beam lithography. Optical applications[23] requiring periodic arrangements of devices are impossible with simple surface deposition. Thus, it is crucial to develop reliable methods for positioning and orienting individual DNA origami (and hence associated devices) on planar substrates.

A variety of techniques now allow the directed assembly of DNA origami on lithographically patterned substrates.[24−33] Strong gold—thiol interactions have been successful in directing one-dimensional DNA origami tubes to create point-to-point connections between gold islands.[29,30] In general, however, methods based on strong

* Address correspondence to
ashwing@caltech.edu,
pwkr@dna.caltech.edu.

Received for review October 21, 2014
and accepted November 20, 2014.

10.1021/nn506014s

electrostatic[28] or strong covalent[32] interactions between DNA and substrate binding sites yield poor orientational precision for two-dimensional origami because origami are fixed quickly, without an opportunity to realign. Weaker electrostatic interactions were used by Kershner *et al.*[25] to position individual DNA origami at binding sites on diamond-like carbon (DLC) and SiO_2 substrates with reasonable yield and orientational precision. However, this "origami placement technique" has been rarely reproduced,[27] or extended,[31] because (i) appropriate DLC substrates are not widely available, (ii) the binding mechanism and experimental conditions for high-quality positioning on SiO_2 substrates have not been well-understood, and (iii) small details of substrate fabrication can have a large effect on placement. Furthermore, the technique required a high (125 mM) Mg^{2+} concentration which causes most components of interest, including carbon nanotubes, metal nanoparticles, and proteins, to aggregate.

RESULTS AND DISCUSSION

Here we build on the basic method of Kershner *et al.*[25] Binding sites of the same shape and size as triangular origami are patterned on an SiO_2 substrate by O_2 plasma etching through a trimethylsilyl (TMS) passivation layer (Figure 1a, Steps 1–5, Supporting Information Figures S1 and S2); this creates silanols which ionize at an appropriate pH to become negatively charged. A solution of origami is applied to the substrate, and Mg^{2+} in the buffer provides an electrostatic bridge between ionized silanols and negatively charged origami (Figure 1b, Method 1). We study, optimize, and extend this placement technique with the goal of making it accessible for a wide variety of applications under diverse experimental conditions. For the basic technique, we achieve both higher orientational precision and a lower working Mg^{2+} concentration than previous studies. We find that the placement yield and quality are highly nonlinear in a number of global (origami concentration, pH, Mg^{2+} concentration, incubation time) and spatial (binding site size and spacing) parameters. Most surprising were the results of varying binding site spacing, which lead to the discovery that the mechanism of binding is not limited to direct diffusion from solution: it also involves an indirect pathway in which origami first bind to unpatterned regions and then undergo 2D diffusion to reach binding sites. Finally, we introduce protocols for placement on positively charged substrates (Figure 1b, Method 2), microcontact printing (Figure 1b, Method 3) and post-placement covalent coupling (Figure 1b, Method 4), which allow the creation and use of DNA origami arrays over a large range of Mg^{2+}-free conditions. A variety of technical details, important to the reproducibility of the technique, are given in the Supporting Information.

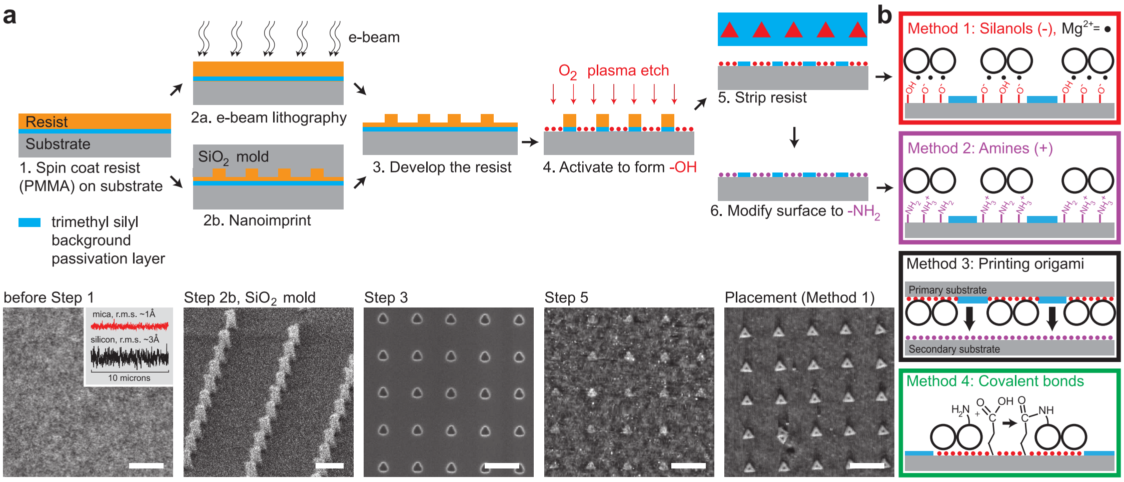

Figure 1. Fabrication of substrates and methods for origami placement and immobilization. (a) Arrays of triangular binding sites are patterned on a SiO_2 substrate *via* e-beam lithography[25] (top, Steps 1–5). An O_2 plasma (Step 4) is used to etch through the trimethysilyl template layer to create silanol groups at each site. AFM or SEM documents how substrates or molds should look at crucial steps (bottom). AFM before lithography (Step 1) shows that substrates are ∼3× as rough as the mica typically used as DNA origami substrates, with an rms roughness of 3 Å. SEM shows the quality of a silicon mold for an alternative patterning method (Step 2b, nanoimprinting[31]) as well as pattern quality in the resist after development (Step 3). AFM after the resist strip (Step 5) shows that binding sites can occasionally be observed by phase imaging, but naked binding sites are difficult to resolve. AFM after placement (Method 1) shows mostly well-oriented single origami. Scale bars, 400 nm. (b) Four variations of placement. Method 1: At an appropriate pH, surface silanols become negatively charged and divalent Mg^{2+} ions can be used as a bridge to immobilize negatively charged DNA origami (black circles). Method 2: Placement without Mg^{2+} can be achieved by functionalizing sites with an amino-terminated silane (Step 6), resulting in lower quality arrays (Figure 4d,e). Method 3: Printing from a substrate made using Method 1 onto an unpatterned amino-terminated surface allows construction of high-quality origami arrays without Mg^{2+} (Figure 4g,g). Method 4: Covalent bonding is another route to Mg^{2+}-free retention of origami: amino-functionalized origami are placed using Method 1, and then the surface is treated with cross-linkers which can form either an amide bond (shown) or an isourea bond (see Figure 4h–k).

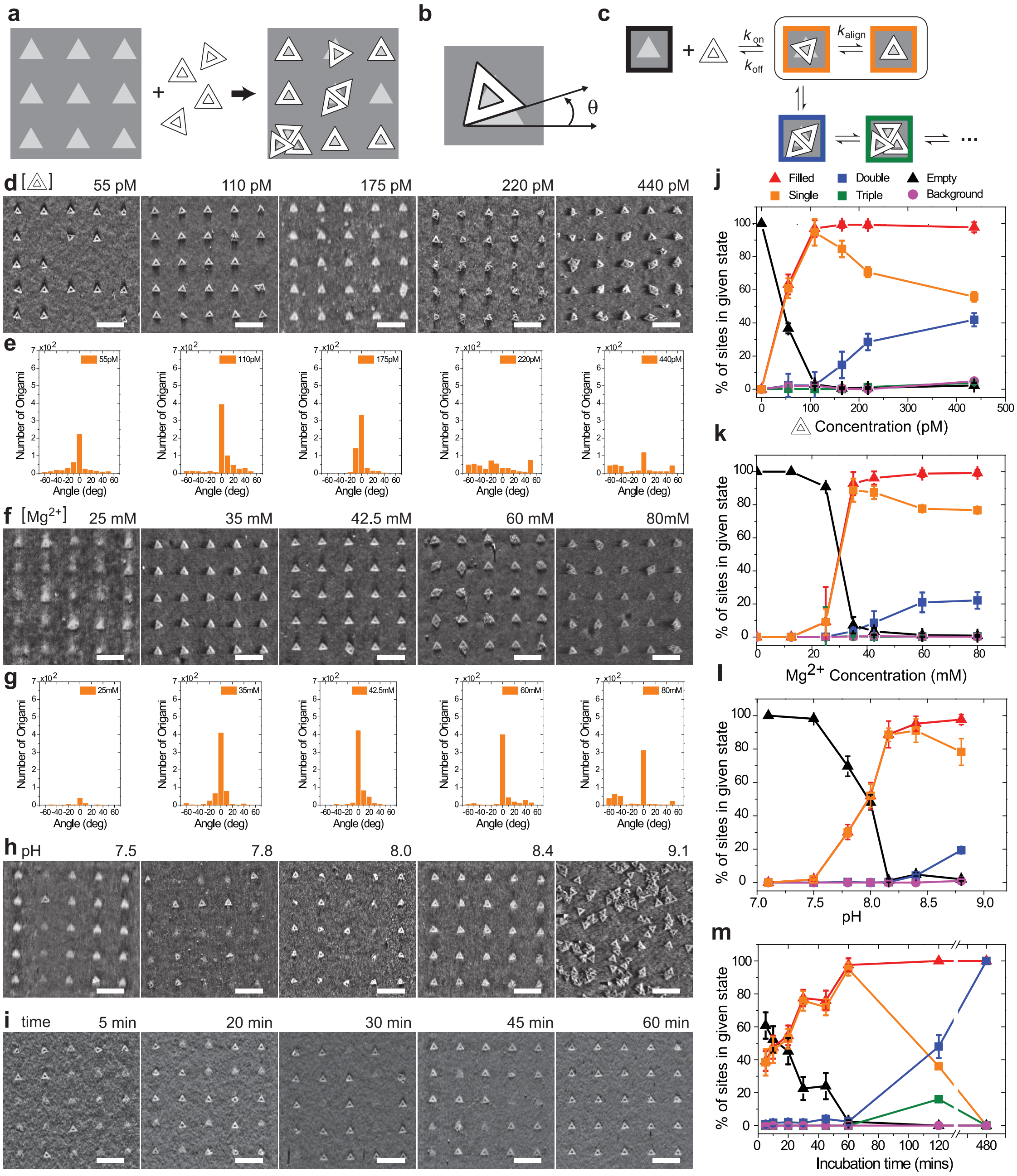

Figure 2. Optimization of origami placement. (a) Schematic shows correct placement, misalignments, vacancies, and multiple binding events. (b) Measurement of origami orientation (θ) relative to its binding site. (c) Model of transitions between the states in (a), assuming that origami arrive from or depart to solution. (d) AFM data and (j) plot showing the nonlinear dependence of placement quality on origami concentration. (f,k) Same for Mg^{2+} concentration, (h,l) for pH, and (i,m) for incubation time. Nonvarying parameters were 110 pM origami, 35 mM Mg^{2+}, pH 8.3, and 60 min incubation (in 5 mM Tris buffer) as applicable. For plots, orange squares show the desired state, a binding site with a single DNA origami. Black triangles show empty sites, and red triangles indicate total occupied sites. (e,g) Histograms show the quality of origami orientation for origami and Mg^{2+} concentration based on (d,f). Error bars are SEM for N = 3 independent replications (of placement, washing, *etc.*) using different chips from the same wafer. 800−1000 binding sites were scored for each replicate. Scale bars, 400 nm.

Effects of Global Parameters. After placement (Supporting Information Figure S3), each binding site can exhibit one of several different states (Figure 2a). A fraction of sites are occupied with single origami in the "correct orientation" in which the origami has maximal overlap with the binding site—the remaining sites may contain a single origami with an incorrect orientation (measured relative to the binding site, Figure 2b), they may contain multiple origami, or they may be empty. Quantitative measurements of the fraction of sites in each state, as well as distribution of orientations, were used to optimize global parameters.

Our initial model of how these states arise during placement is captured in Figure 2c, which depicts a single binding site interacting with origami that bind directly from solution: a single origami may bind with imperfect orientation and realign to the correct orientation, or additional origami may bind to free area on the site before realignment can occur. The mininum free energy state for a single origami is assumed to be the correct orientation, which should maximize the number of silanol$-$Mg^{2+}$-$origami bridges. This model is only intended to be a guide to understanding the sign of the effect of changes made to global parameters, and thus before describing results, we make a few observations regarding the model and placement experiments. Several things prevented us from attempting to extract equilibrium constants or rate constants associated with this model: (i) while binding is weak enough that origami can reorient, it is strong enough that we have been unable to observe a significant dissociation rate, and thus, our experiments are not at equilibrium; (ii) our primary method of observation is fluid-mode AFM, which is highly perturbative, requires strong origami-substrate binding, and does not allow accurate statistics in a weaker binding regime where origami can be knocked off the surface by the AFM tip; and (iii) we will later present evidence that a significant number of origami do not bind sites directly from solution but *via* an indirect pathway which involves them first binding the surface.

Because our experiments were not equilibrium experiments, we chose to measure the state of binding sites after 1 h, a period of time over which initial experiments showed that binding site state evolved from mostly empty to mostly occupied. At 1 h, a series of washes was performed to transfer the sample into an imaging buffer, taking care not to dewet the sample (Supporting Information Figure S4). In particular, washes with the detergent Tween 20 served to prevent further binding and removed origami which were weakly bound to the background or to binding sites (Supporting Information Figure S5). Thus, our measurements likely underestimate the occurrence of single and multiply bound origami during placement, but instead reflect the quality of the complete fabrication process (before drying, Supporting Information Figure S6). AFM movies (Supporting Information movies 1$-$4, 3 frames/s) taken during placement with a less perturbative, fast-scan AFM show multiple binding, unbinding, and realignment, providing direct observation of the processes proposed in Figure 2c; however, it is possible that the observed unbinding and realignment were induced by interaction between the origami and the tip.

We expected that the first parameter we varied, origami concentration (Figure 2d, Supporting Information Figures S7$-$S17), would effect the quality of placement *via* the rate of binding at a site. As origami concentration increases, the rate of origami binding site encounters increases, and second or third origami may bind (essentially irreversibly) before a single origami has a chance to realign and fully occupy the site. This would predict an increase in multiple bindings with increasing concentration, which is reflected in the data by a sharp decrease in single-origami bindings (indicated by orange squares in Figure 2j) as a percent of the number of occupied sites (indicated by red triangles) above 100 pM origami. An unexpected decrease in the quality of alignment of single origami was also observed with increasing concentration (above 100 pM, Figure 2e). Our hypothesis is that the poor alignment of single origami at high concentration actually reflects "cryptic" multiple bindings which have been reduced to single bindings by the Tween 20 wash, which may remove loosely bound second and third origami.

In general, changing a parameter to increase binding strength will decrease k_{off}—this provides a second mechanism to increase multiple bindings since second or third origami will unbind at a low rate. A concomitant increase in cryptic multiple bindings may lead to a decrease in the quality of single-origami alignment, as proposed above. Further, realignment may have an associated activation energy, and increasing binding strength may increase this activation energy and decrease k_{align}, thus providing a second and distinct mechanism for decreasing alignment quality. For the second parameter varied, [Mg^{2+}] (Figure 2f and Supporting Information Figures S18$-$S30), increasing [Mg^{2+}] was expected to increase binding strength by providing more bridges between the origami and negative charges on ionized silanols; thus increased multiple bindings and worse alignment were expected. Both effects were observed: above 35 mM Mg^{2+} multiple bindings increased (Figure 2k) and by 80 mM Mg^{2+} the quality of alignment decreased (Figure 2g).

Similarly, for the third parameter studied, pH (Figure 2h and Supporting Information Figures S31$-$S38), increased [OH$^-$] was expected to increase binding strength by increasing the number of ionized silanols available for Mg^{2+} binding. Indeed, origami binding increased dramatically (Figure 2l) from pH 7.0 to pH 8.4, and multiple bindings increased above pH 8.4. However, at pH 9.1, the TMS groups used to prevent binding of orgami to the background hydrolyzed and origami bound everywhere on the surface. Surface silanols exist in multiple geometries and have varying pK_a:[34] 19% have a pK_a of 4.9, while 81% have a pK_a of 8.5. Thus, the observed increase in origami binding centered at pH 8 is consistent both with the pH at which 50% of silanols are ionized (7.9) and with the pH with the highest rate of change in silanol ionization (8.3), but surface charge, metal$-$surface binding, and eventually DNA$-$surface binding are not solely determined by silanol pK_a: they are also influenced by the specific affinity of a particular metal ion for silanols[35] and DNA, the density of the silanols, and the concentration of competing monovalent and divalent cations in solution.[36,37] Hence we do not conclude that the pK_a of surface silanols will necessarily predict origami behavior for other metal ions or other surfaces.

Lastly, to optimize incubation time, we studied the kinetics of nanoarray formation (Figure 2i and Supporting Information Figures S39–S47). With all other parameters optimized (110 pM origami, 35 mM Mg^{2+}, pH 8.35), we observed that single-origami binding consistently rose to more than 90% at an incubation time of 60 min (Figure 2m), and multiple bindings remained infrequent, at just 5–10% of sites. Further incubation, however, led to a dramatic increase in multiple binding events. By 120 min, ~64% of sites were multiply bound, and by 480 min, the passivating background had undergone significant hydrolyis, origami bound indiscriminantly, and binding sites could not be differentiated from the background. Thus, we chose 60 min as an optimal incubation time. If multiple bindings are more problematic for a downstream application than empty sites, incubation can be arrested early—within 5 min, 40% of sites have single origami and only 2% of sites are multiply bound. The observed kinetics reflect only the binding of origami to sites since dissociation of origami from binding sites has proven unmeasurable: when origami arrays were placed under optimal conditions, washed to remove excess origami, and left under clean buffer for several days, no loss of origami was observed.

Two observations hold for all four parameters studied. First, a fast rise in site occupancy saturates quickly, and in this regime, placement quality is high since most sites hold single origami (Figure 2j–m, orange single-origami traces and red occupied-site traces overlap). For Mg^{2+} and pH, the initial rise was surprisingly fast: from 25 to 35 mM, Mg^{2+} site occupancy jumped from 8 to 96% (Supporting Information Figure S29 shows similar behavior on unpatterned substrates), and from pH 7.5 to pH 8.1, site occupancy jumped from 2 to 92%. Second, after an optimum has been reached, placement quality degrades more slowly, through an increase in multiple binding events (Figure 2j–m, orange traces fall below red). While our optimization highlights the sensitivity of placement quality to all four parameters, careful and precise maintenance of all four parameters enables highly reproducible results. Over the course of 90 independent replications of placement (using chips from four different wafers under optimal conditions, performed over 16 months, for which at least 100 binding sites were measured), we have achieved single-origami binding at 94 ± 4% of sites, with 90% of these origami having an orientation within ±10° of the correct orientation. Further, the similar behavior of placement under each of the four parameters suggests that placement can be reoptimized by adjusting whichever parameter is most convenient—increasing the parameter's value if occupancy is too low, or decreasing the parameter's value if multiple bindings are too high.

We note that the orientational precision achieved here is much better than that previously achieved[25] on Si/SiO_2 substrates (68% of origami within ±20° of the correct orientation) and better than the best precision previously achieved, which was performed on difficult to source DLC substrates (68% of origami within ±10° of the correct orientation). We further note that the optimum concentration we report for Mg^{2+}, 35 mM, is much lower than the concentration previously used[25] for origami placement, 125 mM. We associate this improvement with the addition of a new cleaning step, involving HF/NH_4F treatment,[38] which reduces SiO_2 surface roughness to 3 Å. Placement has not previously been characterized with respect to surface roughness, but we have observed (Supporting Information Figure S30) that thermally grown SiO_2 with 9–10 Å rms roughness requires 90 mM Mg^{2+} to achieve good placement, under otherwise optimized conditions. Further, a surface of intermediate 5 Å roughness required 55 mM Mg^{2+}. Our hypothesis is that a smoother surface may allow a greater number of Mg^{2+} bridges between origami and ionized silanols, but we have not yet ruled out changes to surface chemistry due to the cleaning step.

Placement on thermally grown SiO_2 on Si substrates should enable many electronic device applications, but optical applications such as single-molecule biophysics require transparent substrates. Quartz wafers are one such optically transparent substrate, which is flat (4 Å; glass slides are too rough) and offers surface chemistry similar to thermally grown SiO_2. Unfortunately, quartz is nonconductive, which complicates e-beam lithography. Previously, nanoimprint lithography[31] has been used for origami placement onto SiO_2 on Si substrates under high Mg^{2+} (125 mM) conditions. Initial experiments on quartz using our optimized, lower Mg^{2+} protocol (Step 2b in Figure 1a and Supporting Information Figure S48) suggests that nanoimprint on quartz can achieve placement of equal quality to that created by e-beam on thermally grown SiO_2.

Effects of Spatial Parameters. After optimizing global parameters, we investigated how two spatial parameters—the size and the periodicity of binding sites—affected placement quality. Binding-site size was expected to affect site occupancy, single-origami binding, and alignment; we have only measured the first two. We created a chip with 21 sizes of binding sites, with edge lengths ranging from 15% of the 127 nm origami edge length up to 200%, and performed placement over a range of Mg^{2+} concentrations from 25 to 60 mM (Figure 3a and Supporting Information Figures S49–S55). By varying [Mg^{2+}], our goal was to gain information about the interplay of binding area, the amount of Mg^{2+} available for binding, and binding energy.

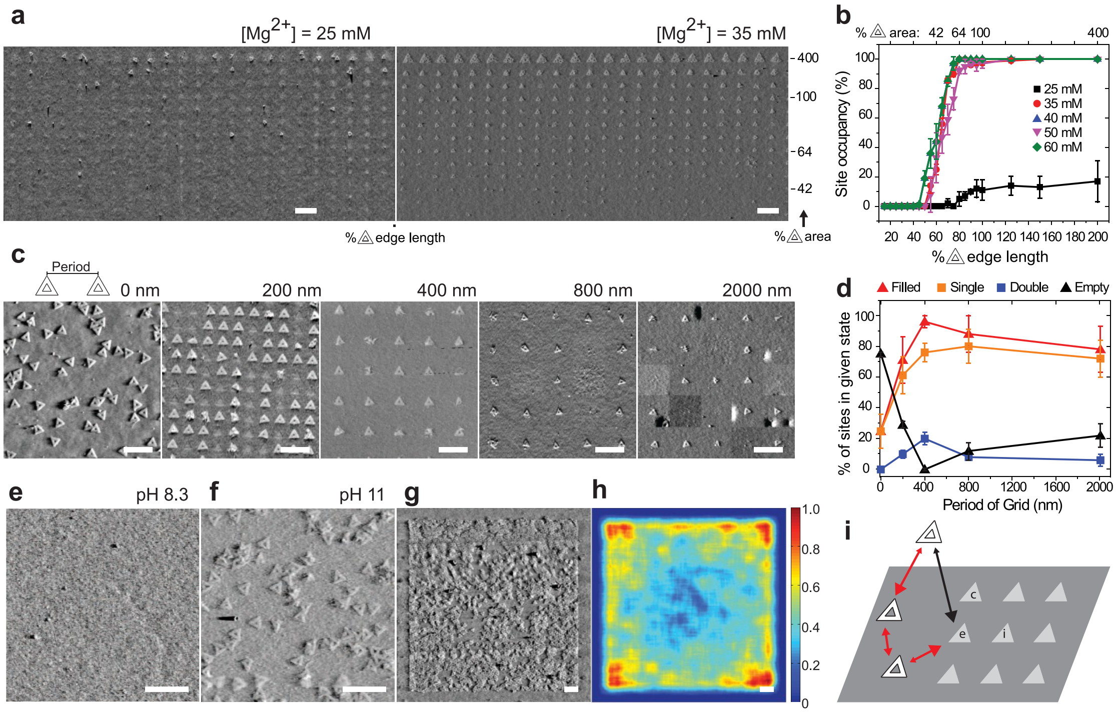

Figure 3. Effects of binding site size and spacing. (a) Binding to triangular sites with 13 different edge lengths ranging from 55 to 200% of the edge length of an origami (127 nm) for two different [Mg^{2+}]. For select sizes, both size as a percentage of edge length and size as a percentage of area (that enclosed by the outer edge of an origami) are noted. (b) Plot of site occupancy (both single and multiple bindings) at five different Mg^{2+} concentrations for 21 different edge lengths from 15 to 200% (error bars are SEM from N = 4 independent replicates). (c) AFM under optimized conditions (110 pM origami, 35 mM Mg^{2+}, pH 8.35 and 60 min) but with different binding-site spacings. For 800 and 2000 nm periods, small regions have been combined into composite images. (d) Plot of binding-site state *vs* period (error bars are SEM from N = 3 independent replicates). (e) AFM of an unpatterned TMS-passivated substrate incubated with 1 nM origami under otherwise optimized conditions and washed with buffer ten times. (f) Chip imaged in (e) after the passivation layer has been removed by increasing the pH to 11. (g) AFM of inhomogeneous binding to a 5 μm × 5 μm activated window, with vacant areas near the center. (h) Probability map calculated from AFM of 25 different 5 μm × 5 μm windows gives the probability of an origami being observed at each position. (i) Model shows direct binding *via* 3D solution diffusion (black arrow) or indirect binding *via* background binding and 2D diffusion (red arrows). Corner (*c*), edge (*e*), and interior (*i*) sites are equivalent for 3D diffusion, but we expect binding rates for corners and edges to higher for 2D diffusion. Scale bars, 400 nm.

Under optimized (35 mM Mg^{2+}, 110 pM origami, pH 8.35, 60 min) conditions, oversized sites were expected to bind multiple origami, and undersized sites were expected to have a lower site occupancy than standard 127 nm sites. This trend was observed (Figure 3b, red trace), but site occupancy saturated (at 100%) for binding sites having an edge length only 80% of the standard size, encompassing only 64% of the total binding area—thus site occupancy is relatively insensitive to a significant undersizing of binding sites. In contrast, single-origami binding events (Supporting Information Figure S55) were maximized (90%) for binding sites that were slightly undersized (85−90% origami edge length). Surprisingly, changing [Mg^{2+}] from 35 to 60 mM had no significant effect: site occupancy saturated at essentially the same binding-site size. Little binding (<20% for all binding-site sizes) was observed at 25 mM Mg^{2+}.

In Figure 2k, site occupancy as a function of [Mg^{2+}] exhibits a Hill coefficient of ∼15, suggesting that Mg^{2+} binding to origami and the surface is highly cooperative. In Figure 3b, the large jump and saturation of site occupancy with increasing [Mg^{2+}] supports cooperative Mg^{2+} binding for site sizes down to 25% of the standard area. The binding-site size variation data also support a picture in which Mg^{2+} forms a layer of defined density and contributes a characteristic binding energy per unit area. Even though equilibrium binding constants cannot be measured, as we have discussed above, binding energy may be reflected in site occupancies observed by AFM because more strongly bound origami can be more stably imaged and better resist being detached by the AFM tip. Assuming that, for a fixed area of overlap between an origami and a site, more Mg^{2+} between the origami and site will translate *via* higher binding energy to a higher site occupancy, then one would predict that higher [Mg^{2+}] should increase site occupancy for undersized sites. Instead, constancy of site occupancy is observed across all site sizes, which suggests that above a threshold concentration of 35 mM Mg^{2+}, the amount of Mg^{2+} per unit area between the origami and the binding site is constant and has reached a maximum value. Such a limit might be set by the density of available ionized silanols, the density of available DNA backbone phosphates, or the interplay between $Mg^{2+}-Mg^{2+}$ repulsion and the geometry of both surface silanols and the DNA backbone, as has been proposed in the "ion correlation model" for DNA−mica binding interactions.[39]

The second spatial parameter studied, the spacing between binding sites, revealed that the mechanism of origami-site binding is much more complex than proposed in our initial model. Under optimized conditions, we examined binding to sites in square arrays with periods from 200 nm up to 2000 nm (Figure 3c and Supporting Information Figures S56−S61). The number of binding sites (∼2 million) was held constant. Additionally, we created a "0 nm" array, in which a 117 μm × 117 μm square patch having the same area as ∼2 million binding sites was fabricated and site occupancy was measured as the number of origami per unit binding-site area. As period increased from 400 to 2000 nm, site occupancy (red) decreased somewhat, from roughly 95 to 80%. This is not a significant trend, and it might be explained because data for larger periods were collected over multiple AFM images, each requiring a separate engage and optimization of conditions to minimize tip−origami interactions—weakly bound origami can be removed from the surface in this process. Single-origami binding (orange) ranged between 75 and 80%. These experiments (included in our overall statistics for single-origami binding) represent the lowest quality placement observed, perhaps because the chips used derive from a different wafer and e-beam write. Below 400 nm, site occupancy dropped quickly—70% for 200 nm and 25% for 0 nm spacings. This suggested that origami-site binding was being negatively affected by the presence of origami at adjacent sites.

We hypothesized that this crowding effect might be mediated by AFM-invisible, weakly bound origami undergoing surface diffusion on the passivated background. To test this, we incubated origami over a completely passivated chip at 10× the standard concentration (1 nM) under otherwise optimized conditions. After 10 buffer washes to remove all free origami from the chip, we imaged the chip by solution AFM and found that no origami could be observed (Figure 3e). Next we hydrolyzed the TMS passivation layer by increasing the pH of the buffer to 11 *via* addition of 0.2 M NaOH. Reimaging revealed a high density of immobilized origami (Figure 3f), which we infer remained weakly bound to the passivation layer during earlier buffer washes; these origami represent ∼42% of the total origami standardly applied to a chip. While surprising, this result is not unprecedented: adsorption and 2D diffusion of DNA hairpins and other molecules on TMS-functionalized surfaces have recently been observed optically.[40,41]

Modeling of 2D diffusion has shown that adsorption on background areas can greatly accelerate the rate of adsorption at specific binding sites.[42] To understand the potential role of surface diffusion here, we simulated placement in two limits (Supporting Information Figure S62): first, conditions under which origami exclusively diffuse in solution in 3D; second, conditions under which all origami immediately condense on the surface and then exclusively diffuse in 2D. Unsurprisingly, in the 3D case, the rate of site occupation is independent of period: 80% site occupancy is reached by 800 time steps for all periods ranging from 0 to 9 lattice sites. However, on a 2D surface, occupied sites block diffusion of origami to unoccupied sites, and so the occupation rate decreases as the period decreases—period 8 reaches 80% site occupancy by 800 time steps, but period 3 requires almost 5000 time steps to reach 80%, and period 0 reaches only 20% occupancy at 5000 time steps. Further, site occupancy is spatially inhomogeneous, with the highest occupancies at the edges of the array. This effect is most extreme in the case of close-packed sites (period 0), for which a narrow band of origami bound at the edge of the array prevents origami from reaching the interior. This result provided a testable prediction for large squares of activated surface (0 nm arrays), and thus we fabricated chips with activated squares whose edges ranged from 500 nm to 5 μm in size. These chips were incubated with origami for 30 min with otherwise optimized conditions (Supporting Information Figure S63). As the size of the squares increased, the size and number of origami-free patches on the interior of squares grew; Figure 3g shows a 5 μm square with several large (>400 nm diameter) vacancies. A probability map (Figure 3h) calculated from the interaction between Mg^{2+} AFM images shows that the probability of an origami being present at a particular position varies from greater than 0.9 at the edge of the square to less than 0.25 at the center. An optical experiment for 20 μm squares gives a similar but nonquantitative result (Supporting Information Figure S63). Experimental spatial inhomogeneities are not as striking as those predicted by the 2D simulation, probably because the experimental results reflect a combination of 3D and 2D diffusion. The fact that 2D diffusion enhances edge and corner binding for large squares suggests that binding rates for corner, edge, and interior sites of nanoarrays should be different (Figure 3i) for closely spaced arrays. Further, it suggests why binding is a function of period for interior sites: as the spacing increases to 400 nm (∼3 origami in size), a site no longer competes with its neighbors for origami diffusing on the background when empty nor blocks origami diffusing to neighbors when occupied. We note that background binding and 2D diffusion cannot be inferred from binding kinetics alone: the Langmuir adsorption model, which assumes exclusively 3D diffusion and independent single-origami binding, fits our incubation time data reasonably well (Supporting Information Figure S64).

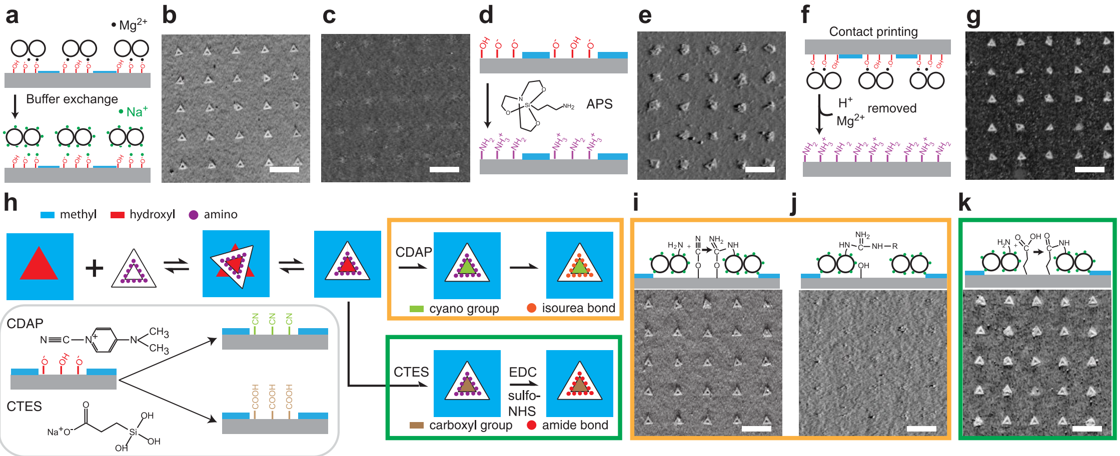

Figure 4. Approaches to Mg^{2+}-free placement. (a–c) Buffer exchange (a) that removes Mg^{2+} and replaces it with Na^+ causes placed origami (b, 5 mM Tris, 35 mM Mg^{2+}, pH 8.3) to be released from the surface (c, 1× PBS, pH 8.3). (d) Amino functionalization *via* aminopropyl silatrane (APS) treatment. (e) Placement on the resulting positively charged surface results in a greater incidence of multple bindings, misalignments, and folding, but is stable in 1× PBS. (f,g) Contact printing (f) from a parent substrate to an amino-functionalized substrate (substrates are clamped together in pure water) preserves the quality of placement and gives stability in 1× PBS (g). (h) Two methods for covalently immobilizing amino-functionalized origami. Origami are placed as usual, and the surface is activated for cross-linking by either a cyanylating (CDAP) or carboxylating (CTES) agent. Cross-linking is either spontaneous (CDAP) or requires a second catalytic step (CTES) using a carbodiimide (EDC) and *N*-hydroxysulfosuccinimide (sulfo-NHS). Inset diagrams surface functionalization reagents. (i) CDAP renders origami stable to 1× PBS and pure water, pH 6.0 (Supporting Information Figure S69). (j) Further addition of a Tris-sodium buffer (5 mM Tris, 150 mM Na^+) aminolyzes the isourea bonds and releases origami. (k) CTES/EDC renders origami stable to pure water, pH 6.0, as well as 1× PBS and Tris (Supporting Information Figure S70).

Maintaining Placement without Mg^{2+}. Origami placed using the normal high Mg^{2+} (35 mM) protocol (Figure 4a,b) simply fall off the surface when washed with Mg^{2+}-free phophate-buffered saline (PBS) at pH 8.3 (Figure 4c). To some extent, lower Mg^{2+} concentration can be compensated by increasing pH after placement if this is compatible with downstream applications. For example, origami are stably attached to SiO_2 in lower Mg^{2+} formation buffer (12.5 mM) at pH ≥9. One approach to achieving truly Mg^{2+}-free placement has been to create positively charged binding sites,[28] achieved through the conversion of surface silanols into positively charged amino groups ($-NH_2$, occurring predominantly as $-NH_3^+$ when significantly below its pK_a of ~10) using a silanization agent such as aminopropyl silatrane[43] (APS, Figure 4d and Supporting Information Figure S65; this compound is much less prone to aggregation than the common amino functionalization agent, (3-aminopropyl)triethoxysilane [APTES]). So far, with such amino-functionalized binding sites (Figure 4e), we have observed (i) a high rate of multiple binding, (ii) poor orientation, and (iii) distortions of origami, such as folding. These observations are consistent with the hypothesis that origami binding to the sites is too strong, and that origami are getting kinetically trapped before they have a chance realign; (i) and (iii) make scoring sites difficult and so we do not quantitatively compare this method to others.

Another approach combines the placement quality afforded by Mg^{2+} binding with the bond stability afforded by a positively charged surface: microcontact printing[44−46] allows origami placed using Mg^{2+} to be transferred to an amino-functionalized surface by bringing the original placement substrate (the stamp) into contact with an amino-functionalized surface and then reducing pH and [Mg^{2+}] to facilitate release from the stamp (Figure 4f). When compared, the resultant nanoarrays (Figure 4g) typically have a slightly smaller site occupancy than that of the stamp (*e.g.*, 91 *vs* 96%, Supporting Information Figure S66) and mild degradation of the alignment (70% within ±10°, *vs* 87%). The periodic grid of original binding sites is well preserved by transfer, and no origami are found off the grid, indicating that origami do not move significantly. Printed nanoarrays are robust to changes in buffer conditions (Figure 4g), as desired. However, the aminated background between origami is highly sticky and may have high nonspecific binding for any devices which might be added downstream—thus devices should be coupled to origami prior to placement and stamping or device-appropriate blocking agents should be used (*e.g.*, noninterfering DNA for DNA-linked objects, or BSA for proteins).

Covalent immobilization of origami after placement offers the most simple route for the creation of nanoarrays that are robust to buffer changes since, unlike stamping, it requires no mechanical manipulation of the substrates. In such an approach, origami are first bound using Mg^{2+} to achieve high-quality placement as usual, and then cross-linking reagents are added to covalently link the origami to the surface. Here, we describe two methods (Figure 4h) which utilize triangular origami bearing an average of 10 primary amines at sites along their inner edge (purple dots Figure 4h, red dots Supporting Information Figure S67). In the first method (Figure 4h, orange box), surface silanols are converted into cyano groups using 1-cyano(4-dimethylamino)pyridinium tetrafluoroborate (CDAP) in a coupling solution created by mixing acetonitrile 50% (v/v) with 5 mM MOPS buffer containing 250 mM Mg^{2+} at pH 7.0. Coupling solution is applied for just 10 min to a chip cooled on ice; a pH of 7.0 is used to increase CDAP activity, and elevated $[Mg^{2+}]$ (150 mM after mixing onto the chip) is used to fix origami stably on the surface at this lower pH. As soon as the cyano group is created, it can spontaneously react with an amino-functionalized origami to form an isourea bond. The isourea derivative so formed is susceptible aminolysis by primary amines.[47] This is why MOPS buffer is used for the coupling reaction rather than buffer containing the amino-bearing Tris base, and this susceptibility enables us to confirm the isourea bond's role in origami immobilization: postcoupling, we first imaged origami in PBS buffer (150 mM Na^+, pH 8.3) to demonstrate that they are stable (for at least an hour) under Mg^{2+}-free conditions (Figure 4i and Supporting Information Figure 68), consistent with the formation of covalent isourea bonds. We next imaged the sample under similar conditions in a buffer that contains 5 mM Tris (150 mM Na^+, pH 8.3) and observed that the origami were completely removed from the surface (Figure 4j).

In a second covalent approach (Figure 4h, black box), carboxyl groups are used to cross-link amino-functionalized origami to the surface using EDC [1-ethyl-3-(3-(dimethylamino)propyl)carbodiimide] catalysis.[47] After standard Mg^{2+}-mediated placement, surface silanols were converted to carboxyl groups by incubating the substrate in a 0.01% (v/v) CTES (carboxyethylsilanetriol) solution. In a second step, carboxyl groups were cross-linked to amino-functionalized origami by incubating the substrate in a coupling buffer (50 mM EDC, 25 mM sulfo-NHS, in 10 mM MOPS, pH 8.1, 125 mM Mg^{2+}). The resulting amide bond is stable (for at least 24 h) in PBS buffer, and unlike the isourea bond, it is stable in Tris-containing buffer (Supporting Information Figure 70). In general, the amide bond should be stable to a wide variety of buffers having a pH between 5 and 9.

Both covalent approaches provide for total removal of salts: the CDAP and CTES/EDC procedures both achieve the stable fixation of origami on substrates under pure water (freshly prepared Milli-Q, nominal pH of 6.0) for at least an hour (Supporting Information Figure 69 and Figure 4k), a condition under which origami would otherwise be completely removed from the surface. Despite the susceptibility of the isourea bond to aminolysis, the CDAP procedure is much simpler, involving a single chemical step and a significant reduction in the number of buffer washes (16 fewer). The CTES/EDC procedure, on the other hand, should be used in cases where the substrate will later be subjected to primary amines (as in the case of Tris buffer), other strong nucleophiles, or high pH.

CONCLUSIONS

Here, we have provided experimental conditions for achieving reproducible, high-quality placement on Si/SiO_2 substrates, along with protocols for noncovalently and covalently stabilized origami nanoarrays under Mg^{2+}-free conditions. By examining the spatial dependence of origami binding, we have revealed that surface diffusion plays an important role in the binding mechanism, one that is crucial to understand for creating nanoarrays of different spacings. With these advances, origami placement should now be widely available for nanotechnological and biophysical applications in a variety of microfabricated devices—deterministic positioning an individual receptor in the heart of a photonic biosensor or a single ligand at the exact end of an AFM tip.

The ability to position individual molecules may also open new doors in chemistry. Origami have been previously used to organize individual reactive chemical groups with ~5 nm precision[13]—each origami serves as an independent nanoscopic reference frame and provides a 100 nm × 70 nm field in which single-molecule reactions can be positioned. Uniquely, our work has used directed self-assembly to deliver individual reactive chemical groups—amines along the inner triangle of the origami—to precise positions on a macroscopic surface, in the laboratory frame of reference. Here the amines were positioned in the service of covalently coupling origami to the surface, but this need not be the case. Looking forward, one can envision uses of placement wherein origami are merely a shuttle, escorting molecular cargo into position for covalent coupling and then departing, leaving behind single molecules precisely located with respect to the laboratory frame—iterative applications of placement might underlie a new type of synthesis with exquisite positional control.

MATERIALS AND METHODS

Origami Formation and Purification. A variation of the "sharp triangle" design described previously[2] was chosen because of its rigidity and low tendency to aggregate. Staple strands (Integrated DNA Technologies, 100 μM each in water) and the scaffold strand (single-stranded M13mp18, Bayou Biolabs, P-107) were mixed together to target concentrations of 100 and 40 nM, respectively (a 2.5:1 staple/scaffold ratio) in 10 mM Tris base, 1 mM EDTA buffer (adjusted to to pH 8.35 with HCl) with 12.5 mM $MgCl_2$. Next, 50 μL volumes of staple/scaffold mixture were heated to 90 °C for 5 min and annealed from

90 to 20 °C at −0.2 °C/min in a PCR machine. DNA LoBind tubes (Eppendorf) (0.5 mL) were used to minimize loss of origami. Amine-functionalized origami were prepared by replacing staples on the inner edge of the triangle with staples extended by 18-base poly-T linkers, to which a 21-base poly-A strands bearing 3′ amine modifications were hybridized. Origami were purified using 100 kDa MWCO spin filters (YM-100, Millipore or Amicon Ultra-0.5 filters with Ultracel-100 membranes).

Fabrication of Placement Substrates. Si (for e-beam) or single-crystal quartz (for nanoimprinting) wafers were purchased from University Wafers. Si wafers were RCA cleaned, immersed in 20 wt % HF (aqueous) for 30 s, immersed in 40 wt % NH_4F (aqueous) for 60 s, washed in deionized water, and baked in a Tystar Tytan furnace at 1000 °C for 3.25 h. This generated a 100 nm thick SiO_2 layer, as verified by a Filmetrics F40 thin-film analyzer. Quartz wafers were cleaned with isopropyl alcohol and blown dry with N_2. Next, both wafer types were coated with trimethylsilyl groups by vapor deposition of HMDS (hexamethyldisilazane). A thin (170−180 nm) layer of poly(methyl methacrylate) diluted in anisole (PMMA 950 A3, Microchem) was spin-coated on the substrate (2500 rpm for 90 s) and baked (at 180 °C for 30 s) for use as a resist during e-beam lithography or nanoimprinting. E-beam was performed with a 100 keV beam delivering a dose of 900 μC/cm^2 at 700 pA, and the resist was developed with a 1:3 solution of methyl isobutyl ketone/isopropyl alcohol (70 s). For nanolithography, a separately fabricated SiO_2 mold was cleaned with isopropyl alcohol and O_2 plasma, coated with tridecafluoro-1,1,2,2-tetrahydooctyl-trichorosilane (Gelest) as a mold release agent, and used to pattern quartz substrates with a Nanonex BX-200 system (100 °C and 500 psi for 30 min). Wafers were cut into 1 cm × 1 cm chips, cleaned with IPA, and activated with an O_2 etch (Plasmatherm Dual Chamber 720/720 RIE) at 50 sccm, 50 mTorr, and 80 W power for 15 s. Resist was stripped by sonicating chips in *n*-methyl pyrrolidone (NMP) at 50 °C for 10 min.

Placement Protocol. Origami were diluted to 110 pM in placement buffer (5 mM Tris, pH 8.35, 35 mM Mg^{2+}), and a 20 μL drop was deposited in the middle of a chip. Chips were placed in a closed 50 mm Petri dish with a moistened kimwipe for 60 min. Origami concentration, incubation time, and buffer pH and [Mg^{2+}] were changed as desired for optimization purposes. After incubation, excess origami were washed away (8×, 60 μL each wash, pipetting up and down 2−3 times per wash) taking care not to dewet the sample. Chips were next washed 5× into Tween washing buffer (5 mM Tris, pH 8.35, 35 mM Mg^{2+}, 0.1% Tween 20) and incubated for 30 min to remove weakly bound origami. To remove Tween 20, the chip is washed 8× into higher pH imaging buffer (5 mM Tris, pH 8.9, 30 mM Mg^{2+}).

AFM Imaging and Analysis. Unless otherwise specified, images were taken in solution tapping mode with a Dimension Icon AFM/Nanoscope V Scanner (Bruker) using the short, fat cantilever from an SNL probe ("sharp nitride lever", 2 nm tip radius, Bruker) resonating at 16−19 kHz. Unless otherwise specified, images are phase images: after engaging, amplitude set point was increased until origami were visible only in the phase channel. This reduced tip−sample interaction. Image were processed using Gwyddion (http://gwyddion.net/).

Microcontact Printing. Origami were placed on SiO_2 (42.5 mM Mg^{2+}, pH 8.35, 110 pM origami, 5 mM Tris, 60 min incubation), and the chip was dried *via* an ethanol series (10 s in each of 25, 50, 70, 80, and 90% ethanol followed by air drying) to create a "master". A second unpatterned SiO_2 substrate (the "copy") was activated with O_2 plasma, incubated with 0.1% APS in water for 20 min, sonicated in DI water, and dried. Master and copy were clamped together, face to face, and immersed in (1) 10 mM phosphate buffer, pH 7.2 for 5 min and (2) DI water for 30 min. At the end of (2), chips were separated while still under water and the copy was imaged under 1× PBS buffer.

CDAP Coupling. After optimized placement, chips were buffer washed (8×, 60 μL each wash, leaving a final 20 μL drop) into MOPS−Mg^{2+} buffer (5 mM MOPS buffer, 250 mM $MgCl_2$, pH 7.0) and put into a Petri dish on ice to cool for 10 min. CDAP (Sigma-Aldrich) solution (250 mg CDAP in 1.5 mL of MOPS−Mg^{2+}) was prepared fresh. Sixty microliters of coupling solution (50% acetonitrile, 50% CDAP solution v/v) was pipetted onto the chip and incubated for 10 min on ice.

CTES/EDC Coupling. CTES (Gelest) stock solution (1% CTES in water) was used to prepare CTES silanization buffer (0.01% CTES in 10 mM Tris, 35 mM Mg^{2+}, pH 8.3) fresh for each experiment. After optimized placement, chips were (1) washed into CTES silanization buffer (8×, 60 μL each wash) and incubated for 2 min, (2) washed 8× to remove CTES (10 mM MOPS, 125 mM Mg^{2+}, pH 8.1), and (3) washed into coupling buffer (50 mM EDC, 25 mM sulfo-NHS, in 10 mM MOPS, pH 8.1, 125 mM Mg^{2+}) and incubated for 10 min.

Conflict of Interest: The authors declare no competing financial interest.

Acknowledgment. We acknowledge financial support from the Army Research Office award W911NF-11-1-0117 and the U.S. National Science Foundation for Expeditions in Computing funding for the Molecular Programming Project (Nos. 0832824 and 1317694, http://molecular-programming.org) and Office of Naval Research Award N000141410702. We acknowledge the gift of aminopropyl silatrane from G. Lovely. We thank S. Guo of Bruker Nano Surfaces for fast scan AFM movies. We thank D. Fygenson, J. Sorensen, T. del Bonis-O'Donnell, S. Woo, and members of Winfree lab for discussions. E-beam lithography was performed in the Kavli Nanoscience Institute at Caltech; nanoimprinting was performed in the UCSB Nanofabrication Facility.

Supporting Information Available: More detailed methods, a troubleshooting guide for placement, origami sequence, and design files, Supplementary Figures 1−70 and Supplementary Movies 1−4 provide additional information regarding the results described throughout the main text. This material is available free of charge *via* the Internet at http://pubs.acs.org.

REFERENCES AND NOTES

1. Seeman, N. C. Nucleic Acid Junctions and Lattices. *J. Theor. Biol.* **1982**, *99*, 237–247.
2. Rothemund, P. W. K. Folding DNA To Create Nanoscale Shapes and Patterns. *Nature* **2006**, *440*, 297–302.
3. Douglas, S. M.; Dietz, H.; Liedl, T.; Högberg, B.; Graf, F.; Shih, W. M. Self-Assembly of DNA into Nanoscale Three-Dimensional Shapes. *Nature* **2009**, *459*, 414–418.
4. Dietz, H.; Douglas, S. M.; Shih, W. M. Folding DNA into Twisted and Curved Nanoscale Shapes. *Science* **2009**, *325*, 725–730.
5. Han, D.; Pal, S.; Nangreave, J.; Deng, Z.; Liu, Y.; Yan, H. DNA Origami with Complex Curvatures in Three-Dimensional Space. *Science* **2011**, *332*, 342–346.
6. Maune, H. T.; Han, S.-P.; Barish, R. D.; Bockrath, M.; Goddard, W. A., III; Rothemund, P. W. K.; Winfree, E. Self-Assembly of Carbon Nanotubes into Two-Dimensional Geometries Using DNA Origami Templates. *Nat. Nanotechnol.* **2010**, *5*, 61–66.
7. Geng, Y.; Pearson, A. C.; Gates, E. P.; Uprety, B.; Davis, R. C.; Harb, J. N.; Woolley, A. T. Electrically Conductive Gold- and Copper-Metallized DNA Origami Nanostructures. *Langmuir* **2013**, *29*, 3482–3490.
8. Ding, B.; Deng, Z.; Yan, H.; Cabrini, S.; Zuckerman, R. N.; Bokor, J. Gold Nanoparticle Self-Similar Chain Structure Organized by DNA Origami. *J. Am. Chem. Soc.* **2010**, *132*, 3248–3249.
9. Dutta, P. K.; Varghese, R.; Nangreave, J.; Lin, S.; Yan, H.; Liu, Y. DNA-Directed Artificial Light-Harvesting Antenna. *J. Am. Chem. Soc.* **2011**, *133*, 11985–11993.
10. Ko, S. H.; Gallatin, G. M.; Liddle, J. A. Nanomanufacturing with DNA Origami: Factors Affecting the Kinetics and Yield of Quantum Dot Binding. *Adv. Funct. Mater.* **2012**, *22*, 1015–1023.
11. Kuzyk, A.; Schreiber, R.; Fan, Z.; Pardatscher, G.; Roller, E.-M.; Högele, A.; Simmel, F. C.; Govorov, A. O.; Liedl, T. DNA-Based Self-Assembly of Chiral Plasmonic Nanostructures with Tailored Optical Response. *Nature* **2012**, *483*, 311–314.

12. Acuna, G. P.; Möller, F. M.; Holzmeister, P.; Beater, S.; Lalkens, B.; Tinnefeld, P. Fluorescence Enhancement at Docking Sites of DNA-Directed Self-Assembled Nanoantennas. *Science* **2012**, *338*, 506–510.
13. Voigt, N. V.; Tørring, T.; Rotaru, A.; Jacobsen, M. F.; Ravnsbæk, J. B.; Subramani, R.; Mamdouh, W.; Kjems, J.; Mokhir, A.; Besenbacher, F.; Gothelf, K. V. Single-Molecule Chemical Reactions on DNA Origami. *Nat. Nanotechnol.* **2010**, *5*, 200–203.
14. Prinz, J.; Schreiber, B.; Olejko, L.; Oertel, J.; Rackwitz, J.; Keller, A.; Bald, I. DNA Origami Substrates for Highly Sensitive Surface-Enhanced Raman Scattering. *J. Phys. Chem. Lett.* **2013**, *4*, 4140–4145.
15. Thacker, V. V.; Herrmann, L. O.; Sigle, D. O.; Zhang, T.; Liedl, T.; Baumberg, J. J.; Keyser, U. F. DNA Origami Based Assembly of Gold Nanoparticle Dimers for Surface-Enhanced Raman Scattering. *Nat. Commun.* **2014**, *5*, 3448.
16. Rajendran, A.; Endo, M.; Sugiyama, H. Single-Molecule Analysis Using DNA Origami. *Angew. Chem., Int. Ed.* **2012**, *51*, 874–890.
17. Qiu, W.; Derr, N. D.; Goodman, B. S.; Villa, E.; Wu, D.; Shih, W.; Reck-Peterson, S. L. Dynein Achieves Processive Motion Using Both Stochastic and Coordinated Stepping. *Nat. Struct. Mol. Biol.* **2012**, *19*, 193–200.
18. Pfitzner, E.; Wachauf, C.; Kilchherr, F.; Pelz, B.; Shih, W. M.; Rief, M.; Dietz, H. Rigid DNA Beams for High-Resolution Single-Molecule Mechanics. *Angew. Chem., Int. Ed.* **2013**, *125*, 7920–7925.
19. Schreiber, R.; Kempter, S.; Holler, S.; Schüller, V.; Schiffels, D.; Simmel, S. S.; Nickels, P. C.; Liedl, T. DNA Origami-Templated Growth of Arbitrarily Shaped Metal Nanoparticles. *Small* **2011**, *7*, 1795–1799.
20. Surwade, S. P.; Zhou, F.; Wei, B.; Sun, W.; Powell, A.; O'Donnell, C.; Yin, P.; Liu, H. Nanoscale Growth and Patterning of Inorganic Oxides Using DNA Nanostructure Templates. *J. Am. Chem. Soc.* **2013**, *135*, 6778–6781.
21. Surwade, S. P.; Zhao, S.; Liu, H. Molecular Lithography through DNA-Mediated Etching and Masking of SiO_2. *J. Am. Chem. Soc.* **2011**, *133*, 11868–11871.
22. Jin, Z.; Sun, W.; Ke, Y.; Shih, C.-J.; Paulus, G. L. C.; Hua Wang, Q.; Mu, B.; Yin, P.; Strano, M. S. Metallized DNA Nanolithography for Encoding and Transferring Spatial Information for Graphene Patterning. *Nat. Commun.* **2013**, *4*, 1663.
23. Holloway, C.; Kuester, E. F.; Gordon, J.; O'Hara, J.; Booth, J.; Smith, D. An Overview of the Theory and Applications of Metasurfaces: the Two-Dimensional Equivalents of Metamaterials. *IEEE Antennas Propag. Mag.* **2012**, *54*, 10–35.
24. Kuzyk, A.; Yurke, B.; Toppari, J. J.; Linko, V.; Törmä, P. Dielectrophoretic Trapping of DNA Origami. *Small* **2008**, *4*, 447–450.
25. Kershner, R. J.; Bozano, L. D.; Micheel, C. M.; Hung, A. M.; Fornof, A. R.; Cha, J. N.; Rettner, C. T.; Bersani, M.; Frommer, J.; Rothemund, P. W. K.; *et al.* Placement and Orientation of Individual DNA Shapes on Lithographically Patterned Surfaces. *Nat. Nanotechnol.* **2009**, *4*, 557–561.
26. Gerdon, A. E.; Oh, S. S.; Hsieh, K.; Ke, Y.; Yan, H.; Soh, H. T. Controlled Delivery of DNA Origami on Patterned Surfaces. *Small* **2009**, *5*, 1942–1946.
27. Hung, A. M.; Micheel, C. M.; Bozano, L. D.; Osterbur, L. W.; Wallraff, G. M.; Cha, J. N. Large-Area Spatially Ordered Arrays of Gold Nanoparticles Directed by Lithographically Confined DNA Origami. *Nat. Nanotechnol.* **2010**, *5*, 121–126.
28. Gao, B.; Sarveswaran, K.; Bernstein, G. H.; Lieberman, M. Guided Deposition of Individual DNA Nanostructures on Silicon Substrates. *Langmuir* **2010**, *26*, 12680–12683.
29. Ding, B.; Wu, H.; Xu, W.; Zhao, Z.; Liu, Y.; Yu, H.; Yan, H. Interconnecting Gold Islands with DNA Origami Nanotubes. *Nano Lett.* **2010**, *10*, 5065–5069.
30. Pearson, A. C.; Pound, E.; Woolley, A. T.; Linford, M. R.; Harb, J. N.; Davis, R. C. Chemical Alignment of DNA Origami To Block Copolymer Patterned Arrays of 5 nm Gold Nanoparticles. *Nano Lett.* **2011**, *11*, 1981–1987.
31. Penzo, E.; Wang, R.; Palma, M.; Wind, S. J. Selective Placement of DNA Origami on Substrates Patterned by Nanoimprint Lithography. *J. Vac. Sci. Technol., B* **2011**, *29*, 06F205.
32. Scheible, M. B.; Pardatscher, G.; Kuzyk, A.; Simmel, F. C. Single Molecule Characterization of DNA Binding and Strand Displacement Reactions on Lithographic DNA Origami Microarrays. *Nano Lett.* **2014**, *14*, 1627–1633.
33. Teshome, B.; Facsko, S.; Keller, A. Topography-Controlled Alignment of DNA Origami Nanotubes on Nanopatterned Surfaces. *Nanoscale* **2014**, *6*, 1790–1796.
34. Dong, Y.; Pappu, S. V.; Xu, Z. Detection of Local Density Distribution of Isolated Silanol Groups on Planar Silica Surfaces Using Nonlinear Optical Molecular Probes. *Anal. Chem.* **1998**, *70*, 4730–4735.
35. Dishon, M.; Zohar, O.; Sivan, U. Effect of Cation Size and Charge on the Interaction between Silica Surfaces in 1:1, 2:1, and 3:1 Aqueous Electrolytes. *Langmuir* **2011**, *27*, 12977–12984.
36. Cheng, H.; Zhang, K.; Libera, J. A.; Olvera de La Cruz, M.; Bedzyk, M. J. Polynucleotide Adsorption to Negatively Charged Surfaces in Divalent Salt Solutions. *Biophys. J.* **2006**, *90*, 1164–1174.
37. Libera, J. A.; Cheng, H.; Olvera de la Cruz, M.; Bedzyk, M. J. Direct Observation of Cations and Polynucleotides Explains Polyion Adsorption to Like-Charged Surfaces. *J. Phys. Chem. B* **2005**, *109*, 23001–23007.
38. Becker, J.; Pysch, D.; Leimenstoll, A.; Hermle, M.; Glunz, S. Wet-Chemical Pre-treatment of c-Si Substrates Enhancing the Performance of a-Si: H/c-Si Hetero-Junction Solar Cells. 24th European PV Solar Energy Conference and Exhibition, Hamburg, Germany. **2009**.
39. Pastré, D.; Piétrement, O.; Fusil, S.; Landousy, F.; Jeusset, J.; David, M.-O.; Hamon, L.; Cam, E. L.; Zozime, A. Adsorption of DNA to Mica Mediated by Divalent Counterions: A Theoretical and Experimental Study. *Biophys. J.* **2003**, *85*, 2507–2518.
40. Kastantin, M.; Schwartz, D. K. DNA Hairpin Stabilization on a Hydrophobic Surface. *Small* **2013**, *9*, 933–941.
41. Skaug, M. J.; Mabry, J.; Schwartz, D. K. Intermittent Molecular Hopping at the Solid–Liquid Interface. *Phys. Rev. Lett.* **2013**, *110*, 256101.
42. Wang, D.; Gou, S.-Y.; Axelrod, D. Reaction Rate Enhancement by Surface Diffusion of Adsorbates. *Biophys. Chem.* **1992**, *43*, 117–137.
43. Shlyakhtenko, L. S.; Gall, A. A.; Filonov, A.; Cerovac, Z.; Lushnikov, A.; Lyubchenko, Y. L. Silatrane-Based Surface Chemistry for Immobilization of DNA, Protein–DNA Complexes and Other Biological Materials. *Ultramicroscopy* **2003**, *97*, 279–287.
44. Lange, S. A.; Benes, V.; Kern, D. P.; Hörber, J. H.; Bernard, A. Microcontact Printing of DNA Molecules. *Anal. Chem.* **2004**, *76*, 1641–1647.
45. Kaufmann, T.; Ravoo, B. J. Stamps, Inks and Substrates: Polymers in Microcontact Printing. *Polym. Chem.* **2010**, *1*, 371–387.
46. Han, S.-p.; Maune, H. T.; Barish, R. D.; Bockrath, M.; Goddard, W. A., III. DNA-Linker-Induced Surface Assembly of Ultra Dense Parallel Single Walled Carbon Nanotube Arrays. *Nano Lett.* **2012**, *12*, 1129–1135.
47. Janson, J.-C. *Protein Purification: Principles, High Resolution Methods, and Applications*; John Wiley & Sons: New York, 2012; Vol. 151.